Available online at www.sciencedirect.com
ScienceDirect
Ceramics International 36 (2010) 623–634
CERAMICS INTERNATIONAL
www.elsevier.com/locate/ceramint

The effect of citric acid on the sintering of calcium phosphate bioceramics

Anastasios I. Mitsionis [a], Tiverios C. Vaimakis [a,*], Christos C. Trapalis [b]

[a] *Department of Chemistry, University of Ioannina, P.O. Box 1186, Ioannina 451 10, Greece*
[b] *"Demokritos" National Centre for Scientific Research, Institute of Materials Science, Athens 153 10, Greece*

Received 6 July 2009; received in revised form 28 August 2009; accepted 24 September 2009
Available online 29 October 2009

Abstract

Biphasic calcium phosphate particles were prepared using a rapid increase of the pH value by adding an amount of concentrated ammonia solution, into a well-mixed solution containing $Ca(H_2PO_4)_2{\cdot}H_2O$ and $CaCl_2$ with Ca/P = 1.667 molar ratio; with or without the presence of citric acid (CiA). The precipitation of Calcium Phosphates took place at 97 °C using high-speed dispersing equipment. The samples were characterized using XRD, FT-IR, BET and SEM techniques. The thermal behaviour was studied by TG, DTG and DTA techniques. The modified precipitation method leads to the formation of biphasic needle-like particles consisted of crystalline hydroxyapatite (HA) and β-tricalcium phosphate (β-TCP). The presence of CiA in the initial solution leads to the formation of aggregated nonporous small spheroidal particles consisted of low crystallinity phases of HA and octacalcium phosphate (OCP). The later facilitates the sintering process. The calcined samples at 900 °C were consisted of calcium pyrophosphate (CPP) and TCP. α-TCP is formed in the presence of a large amount of calcium citrate complexes. The main sintering process took place at the temperature range between 750 and 1150 °C, which were strongly depended on the initial amount of the CiA in the precipitation process. These results indicated that the citrate presence in the initial solution have a strong influence on the nucleation and growth processes by complexation with calcium ions and incorporation into the solid structure during particle growth.

Keywords: A. Powders: chemical preparation; Citric acid; Hydroxyapatite B; Sintering; Calcium phosphate; Thermal decomposition

1. Introduction

Hydroxyapatite (HA) is one of the most common ceramics that can be used as artificial implant for medical purposes. There are many applications for bioceramics because of their biocompatibility and chemical similarity to the human hard tissue. Nowadays there are many efforts on improving the mechanical properties and the material performance at prostheses in the human body. HA is also being tested as an absorbent for organic molecules that exist inside the human body. It is well known that organic modifiers are widely used in the morphology and size-controlled synthesis of HA [1–6].

Citric acid (CiA) is a major natural organic compound involved in many biochemical activities (Krebs cycle); furthermore it is an ingredient of the human hard tissue (about 1 wt.%). Citric acid is believed to affect the formation of human bone by adsorbing in both the reacting and the producing phases of calcium ions [7].

There is a large interest in the transformation of calcium phosphates in the presence of CiA because of their biomedical importance. The addition of CiA in the initial steps of bone apatite formation has many consequences in the final product. CiA in a calcium containing solution acts as an entrapment agent for calcium ions [8,9]. Citrate ions were found to reduce the rates of precipitation due to both their complexation with Ca^{2+} ions and their adsorption on the surface of the formed particles; thus blocking some active growth centers [10]. Among the precursors used, CiA is a strong complex forming agent and can form stable complex compounds especially under acidic condition [11]. The shape and the composition of calcium phosphate crystals depend on the preparation process [12–14]. The presence of citrate anions in the simulated milk ultrafiltrate (SMUF) test solution [15] leads to the formation of HA, while in the absence of the citrate ions plate-like brushite is precipitated [16].

The sintering temperature is also a critical factor for improving the mechanical properties of HA that influences the phase stability, densification behaviour, microstructure, such as particle size and shape as well as particle size distribution, and hence the hardness of HA ceramics [17–23]. Although, the

---

* Corresponding author. Tel.: +30 2651098352; fax: +30 2651098795.
E-mail address: tvaimak@cc.uoi.gr (T.C. Vaimakis).

0272-8842/$36.00 © 2009 Elsevier Ltd and Techna Group S.r.l. All rights reserved.
doi:10.1016/j.ceramint.2009.09.034

beginning of shrinkage and the densification of HA depend mainly on the Ca/P ratio, the final sintering density depends on the particle size, the homogeneity and the agglomeration character of the powder precursor [24]. In our previous paper [25] we prepared lath-like HA particles using a modified precipitation method and we found that the calcination decreases the particles length and changes the particles morphology to spherical shape. It was found that long aging time of the slurry favours the formation of thermally stable HA particles. Sintering of compacted powders begins at temperatures higher than 900 °C.

In the present work we studied the effect of the addition of CiA in the preparation of HA with a modified precipitation method [26]. According to this method HA is prepared by a rapid increase of the pH value of a solution containing calcium and phosphate ions with molar ratio similar to HA following the addition of various amounts of CiA, using a high-speed dispersing equipment (HSDE). Afterwards the powders prepared were studied using X-ray diffractometry (XRD), thermogravimetry/differential thermal analysis (TG/DTA), thermomechanical analysis (TMA-thermodilatometry, TD), scanning electron microscopy (SEM), Fourier-transform infrared spectroscopy (FT-IR) and N_2 adsorption–desorption porosimetry.

2. Materials and methods

2.1. Materials

The reagents that have been used were $CaCl_2 \cdot 2H_2O$ (Fluka, Assay (KT) 99%), $Ca(H_2PO_4)_2 \cdot H_2O$ (Riedel-de Haën, Assay 88%), Citric Acid (Riedel-de Haën, Asssay 99.5%) and Ammonia solution 25% (Riedel-de Haën).

2.2. Preparation

The apparatus used was described in our previous work [26] and consisted of a 1 L glass reactor vessel with a four neck cover, a dispersing equipment (Model S 50 KG-HH, IKA-Works) with dispersed element (Model G 45M, IKA-Works, Inc., Wilmington, NC) and heating mantle. The reaction temperature was adjusted by a temperature controller, which was connected to a thermocouple. A flowing stream of air was used to remove CO_2 from the reactor. The air was passed through an absorption tube containing solid NaOH as a CO_2 absorbent. A condenser and a proper syringe containing concentrated NH_4OH solution were connected to the one angled side neck. An 800 mL solution of 0.0538 mol of $Ca(H_2PO_4)_2 \cdot H_2O$ and 0.1254 mol of $CaCl_2 \cdot 2H_2O$ with a Ca/P molar ratio of 1.67 (the stoichiometry of HAp) as well as different amounts of CiA, in order to create solutions with a molar ratio of CiA/Ca equal to 0.025, 0.050, 0.075, 0.100, as it is shown in Table 1, was transferred into the reactor vessel and was heated to 97 °C using an airflow rate of 15 L/h for 30 min. The rotation speed of the disperser was adjusted to 5000 rpm, and then 15 mL of concentrated NH_4OH solution (25%, w/w) was added at once using the syringe. The solution pH increased from 3.2 to 8.8 and white slurry was produced. The slurry was aged under the above mentioned conditions for 30 min. Subsequently, the mixtures were cooled to room temperature, filtrated, washed with distilled water, and dried at 90 °C for 1 day. The as prepared samples were calcined at 900 °C for 3 h.

Table 1
Molar ratio and specific surface area of samples. Initial Ca/P ratio = 1.67.

Run	Sample's code	CiA/Ca ratio	Calcination at 900 °C	Specific surface area (m^2/g)
1	R0	0.000	No	60
2	R25	0.025	No	109
3	R50	0.050	No	152
4	R75	0.075	No	168
5	R100	0.100	No	172
6	C0	0.000	Yes	82
7	C25	0.025	Yes	10
8	C50	0.050	Yes	8
9	C75	0.075	Yes	5
10	C100	0.100	Yes	2

2.3. Characterization

The identification of the crystal phases in the obtained products was carried out by the X-ray diffraction (XRD) technique, using a Brüker P8 Advance apparatus, with a 2θ range of 20–60° in steps of 0.02° and the identification of the patterns was made by the cards of the International Centre for Diffraction Data (ICDD). FT-IR was performed using a spectrophotometer (Model Spectrum RX I FT-IR, Perkin–Elmer). The KBr disk technique was used with ~2 mg of powder in ~200 mg of spectroscopic-grade KBr (Merck), which had been dried at 100 °C. Infrared spectra were recorded in the 4000–400 cm^{-1} region.

The textural properties of the solids were examined by N_2 adsorption–desorption porosimetry which provides also the pore size distribution, using a Fisons Instruments Sorptomatic 1900, and scanning electron microscopy (SEM), using a JEOL JSM-6300 instrument. Before N_2 adsorption–desorption measurement the sample was degassed at 150 °C and pressure of 10–30 Torr for 6 h.

2.4. Thermal analysis

Simultaneously TG/DTA (thermogravimetry/differential thermal analysis) measurements were carried out by a STA 449C (Netzch-Gerätebau, GmbH, Germany) thermal analyzer. The heating range was from ambient temperature up to 1200 °C, with a heating rate of 10 °C/min under synthetic air flow rate of 30 cm^3/min. As reference Al_2O_3 powder was used. For sintering analysis, the powder samples were uniaxially pressed in a cylindrical die, with diameter of 6 mm, under a 350 MPa compressing stress. Linear shrinkage (thermodilatometry, TD) was determined with a NETZSCH horizontal dilatometer (Model TMA/DIL 402C), using the same thermal cycle as the one used for TG-DTA techniques (i.e. a heating rate of 10 °C/min). The differential thermogravimetric (DTG) and differential thermodilatometric (DTD) curves were obtained by differentiation of corresponding TG and TD curves, using the NETZSCH SOFTWARE FOR THERMAL ANALYSIS (Version 3.6), while the peak separation of the DTG and DTD curves was performed using NETZSCH SEPARATION OF PEAKS software (SW/PKS/650.01A).

3. Results and discussion

3.1. XRD analysis

Fig. 1 shows the XRD patterns of uncalcined phosphate materials. The XRD pattern of the sample prepared without the presence of CiA containing strong and sharp peaks corresponding characteristically to HA and β-tricalcium phosphate (β-TCP) (File No. 84-1998 and 70-2065, respectively, International Centre for Diffraction Data (ICDD), Newtown Square, PA). In our previous paper [26] dropwise addition of ammonia solution led to the formation of only one phase; high crystallinity HA. From the XRD results in this paper, we suggest that the rapid pH increase of a well-mixed solution in order to obtain quickly a supersaturated solution produces well-crystallized biphasic material with general Ca/P atomic ratio lower than the initial value of 1.67 (the TCP has Ca/P atomic ratio equal to 1.50). On the other hand aging time was not sufficient to hydrolyse the TCP crystals to HA one.

The presence of CiA in the initial solution resulting to the formation of very low crystallinity phases of HA and octacalcium phosphate (OCP, $Ca_8(HPO_4)_2(PO_4)_4{\cdot}5H_2O$). The CiA acts as an entrapping agent of Ca ions resulting to the formation of OCP with lower Ca/P atomic ratio (Ca/P = 1.33) than TCP. Previous studies indicated that the high reaction temperature and the mechanical activation induced from the dispersing equipment produce high crystallinity material [26]. In this work the presence of calcium citrate complexes rebut the effect of the above mentioned factors and led to the formation of low crystallinity HA and OCP phases. Amorphous calcium phosphate (ACP) also has been prepared by rapid precipitation at pH 8.9, 9.9 and 11.7 with formulae $Ca_{8.58}(HPO_4)_{1.11}(PO_4)_{4.89}(OH)_{0.27}$, $Ca_{9.00}(HPO_4)_{0.16}(PO_4)_{5.84}(OH)_{0.16}$ and $Ca_{9.21}(HPO_4)_{0.08}(PO_4)_{5.92}(OH)_{0.50}$ [27]. The conversion of the soluble CaP compounds into calcium-deficient apatite (CDA) is favoured by the thermodynamic stability of the apatite phase in basic media. The composition of the resulting CDA depends on a wide range of factors (temperature, pH, concentrations and rate of mixing). Depending on these parameters, the composition of the CDA may vary, leading to mixtures of β-TCP and HA phases when heated at more than 800 °C [28]. An ACP corresponding to an amorphous OCP which was prepared at 37 °C by rapid precipitation from an alcoholic solution has been reported [29].

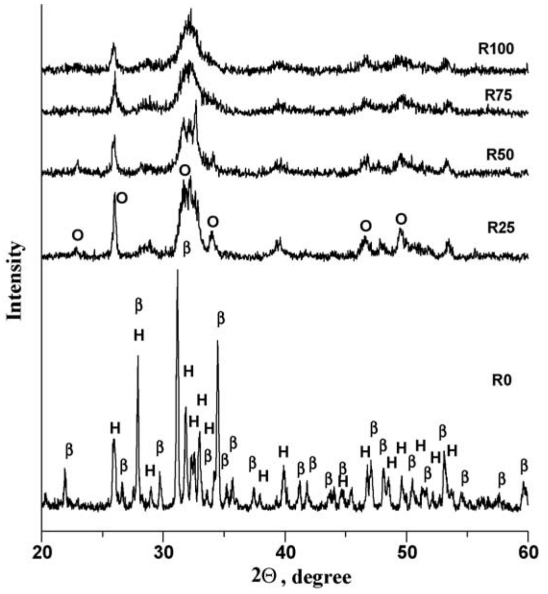

Fig. 1. XRD powder patterns of raw non-calcined calcium phosphate materials. H: HAp; β: β-TCP; O: OCP.

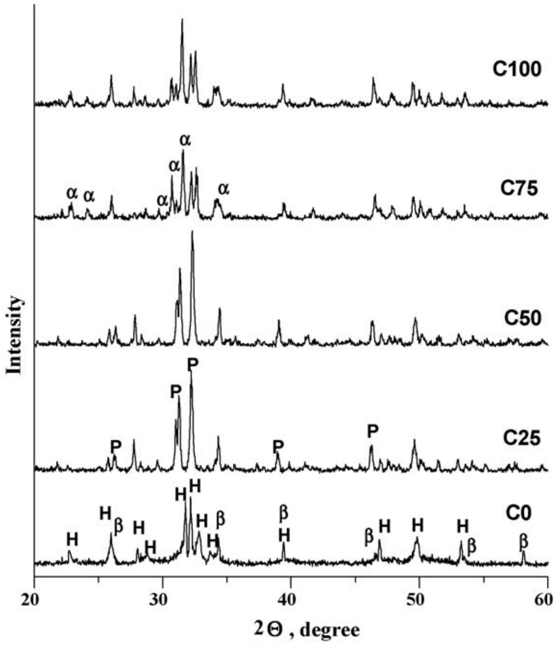

Fig. 2. XRD powder patterns of calcined calcium phosphate materials. H: HAp; β: β-TCP; α: α-TCP; P: calcium pyrophosphate.

On the contrary the calcined samples presented in Fig. 2 show better crystalline phases. The XRD pattern of the sample prepared without the presence of CiA contains strong and sharp peaks that correspond characteristically to HA and β-TCP, similar to the uncalcined one. The XRD patterns C25 and C50 (Fig. 2) show that except from β-TCP phase, a substantial amount of calcium pyrophosphate (CPP, $Ca_2P_2O_7$, File No. 70-0881, ICDD) is recorded after calcination at 900 °C. The corresponding diffraction lines are very sharp; indicating high crystallization of the CPP and β-TCP phases. Due to the absence of OCP and HA from the XRD patterns of C25 and C50 samples (see Table 1), we assumed that the formation of CPP comes from the decomposition of OCP (reaction (1)), while simultaneously the HA react with CPP produced TCP (reaction (2)). The XRD patterns (Fig. 2) of C75 and C100 samples (see Table 1) show that after calcination at 900^0C the produced phases were α-TCP (File No. 70-70-0364, ICDD) and CPP phases.

The amorphous calcium phosphate (ACP) prepared by precipitation from solution with low initial ion concentrations, during heating tended to first crystallize β-TCP, while from high ion concentrations initial α-form is produced. The ion concentrations of initial solution were high with a [Ca] × [P] product of ~30×10^3 mM^2, and we expect firstly the crystallization into α-TCP, with an exothermic peak at about 660 °C followed by an exothermic conversion of α-TCP into β-form at about 870 °C [30]. With further heating the α-form of TCP is formed after calcination of β-form at about 1200 °C. The presence of α-TCP after heating at 900^{0}C is attributed to the idiomorphic structure of the uncalcined sample, due to the presence of a large amount of calcium citrate complexes and OCP with molar ratio of Ca/P equal to 1.33. The α-TCP is related to the structure of apatite, and can be seen from the consideration of its unit cell's dimensions with those of apatite. α-TCP has a "looser" structure than β-TCP, and consequently has higher internal energy and chemical reactivity [31]:

$$\mathrm{Ca_8(HPO_4)_2(PO_4)_4 \cdot }n\mathrm{H_2O} \rightarrow \mathrm{2Ca_3(PO_4)_2 + Ca_2P_2O_7} + (n+1)\mathrm{H_2O} \qquad (1)$$

$$\mathrm{Ca_{10}(PO_4)_6(OH)_2 + Ca_2P_2O_7 \rightarrow 4Ca_3(PO_4)_2 + H_2O} \qquad (2)$$

3.2. FT-IR

Fig. 3 shows the FT-IR absorption spectrum of uncalcined sample without the presence of CiA (R0 curve). In general, the spectrum is in accordance with the literature. The broad band at 3100–3500 cm^{-1} corresponds to adsorbed hydrate, while a weak sharp peak at 3575 cm^{-1} corresponds to the stretching vibration of the lattice OH$^-$ ions. The weak shoulder at 1255 cm^{-1} and a weak peak at 872 cm^{-1} can be assigned to P–O–H in-plane and out-of-plane deformation modes, respectively, which indicates the presence of the ionic group $\mathrm{HPO_4}^{2-}$, in other words, the formation of CDA. The characteristic bands for $\mathrm{PO_4}^{3-}$appear at 470, 560, 602, 960 and 1030 cm^{-1}. A medium sharp peak at 1400 cm^{-1} is assigned to the carbonate vibration.

FT-IR spectras of samples prepared in the presence of CiA in the initial solution show some new vibrations. Two weak peaks at 2923 and 2851 cm^{-1} are attributed to C–H vibrations of citrate complexes (Fig. 3b). A very broad peak at ~1600 cm^{-1}, a shoulder at ~1450 cm^{-1} as well as a sharp and weak at 1387 cm^{-1} (R50, R75 and R100 samples, see Table 1) are characteristic of the carboxyl stretching vibrations of citrate complexes (Fig. 3c) [19,32–34]. In addition to these, a shoulder band at ~3200 cm^{-1} can be ascribed to ammonium ions ($\mathrm{NH_4}^+$) [34], which adsorbed on the solid from the initial solution. In the precipitation method, the ammonium are not incorporated into the apatite lattice but, rather, adsorbed onto the CaP precipitates and eliminated by heating above 400 °C [28].

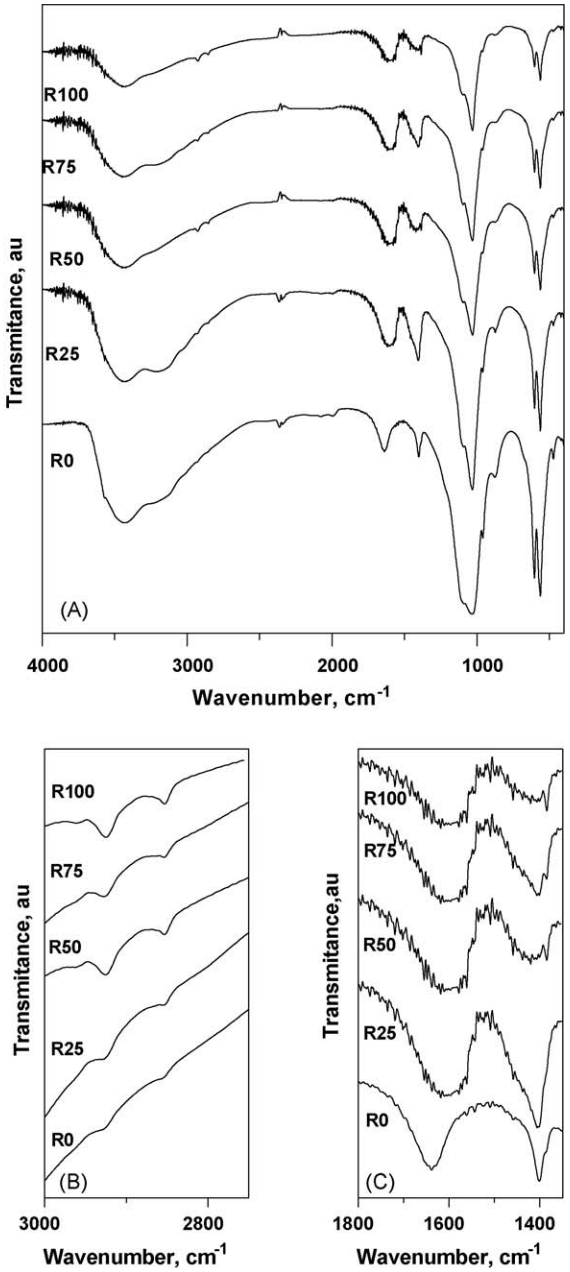

Fig. 3. Ft-IR spectras of raw calcium phosphate materials.

3.3. Thermal analysis

Fig. 4 shows the TG, DTG and DTA curves of non-calcined calcium phosphate sample. The thermal transformation of sample prepared in absence of CiA takes place through four not well-distinguished steps. The first step is an endothermic peak on the DTA curve between room temperature and ~180 °C. It consisted of two stages, as reveal the peak separation (deconvolution) of DTG curve (Fig. 4b and Table 2, peaks 1 and 2), and it can be attributed to removal of absorbed and/or crystalline water as well as of other adsorbed volatile compounds (reaction (3)):

$$\mathrm{Ca}_{10-x}(\mathrm{HPO_4})_x(\mathrm{PO_4})_{6-x}(\mathrm{OH})_{2-x}\cdot n\mathrm{H_2O} \rightarrow \mathrm{Ca}_{10-x}(\mathrm{HPO_4})_x(\mathrm{PO_4})_{6-x}(\mathrm{OH})_{2-x} + n\mathrm{H_2O} \qquad (3)$$

The transformation of acid-phosphate ions to pyrophosphate, take place between 180 and 700 °C during a second endothermic step (reaction (4)). The deconvolution of DTG curve shows that the second step, also, consists from two stages

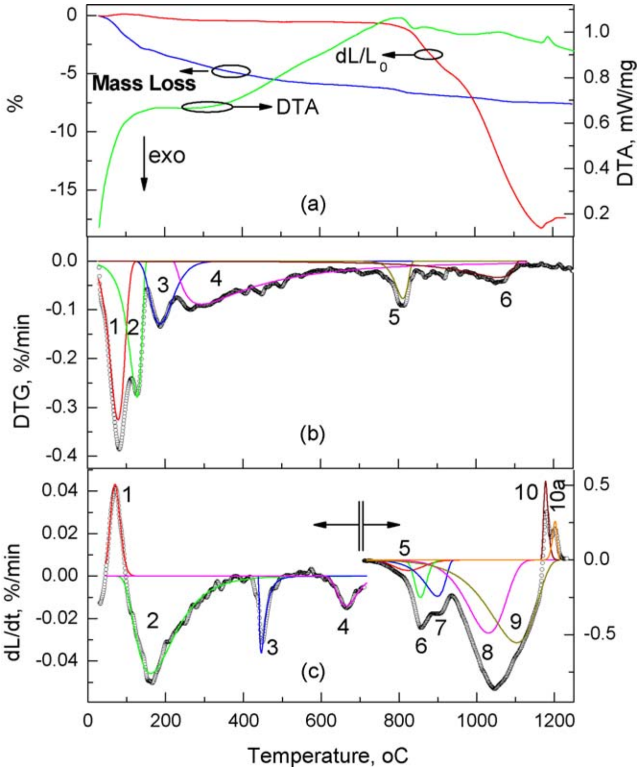

Fig. 4. TG, DTA and linear shrinkage curves (a), as well as the peak separation of DTG (b) and differential linear shrinkage (c) curves of R0 sample.

(Fig. 4b and Table 2, peaks 3 and 4), indicates the presence two different acid-phosphate structural groups. In the same temperature range there are two small peaks at temperature 447 and 498 °C, respectively:

$$\mathrm{Ca}_{10-x}(\mathrm{HPO}_4)_x(\mathrm{PO}_4)_{6-x}(\mathrm{OH})_{2-x} \rightarrow \mathrm{Ca}_{10-2x}(\mathrm{PO}_4)_{6-x}(\mathrm{OH})_{2-x} + (x/2)\mathrm{Ca}_2\mathrm{P}_2\mathrm{O}_7 + (x/2)\mathrm{H}_2\mathrm{O} \qquad (4)$$

A narrow and sharp peak in temperature range between 770 and 835 °C (Fig. 4b and Table 2, peak 5) is attributed to the transformation of pyrophosphate to TCP (reaction (5)):

$$\mathrm{Ca}_{10-2x}(\mathrm{PO}_4)_{6-x}(\mathrm{OH})_{2-x} + (x/2)\mathrm{Ca}_2\mathrm{P}_2\mathrm{O}_7 \rightarrow \mathrm{Ca}_{10-5x/2}(\mathrm{PO}_4)_{6-x}(\mathrm{OH})_{2-2x} + (x/2)\mathrm{Ca}_3(\mathrm{PO}_4)_2 + (x/2)\mathrm{H}_2\mathrm{O} \qquad (5)$$

The partial dehydration (reaction (6)) and the decomposition of HAp (reaction (7)) take place in the forth step at the temperature range between ~850 and ~1100 °C (Fig. 4b and Table 2, peak 6). In the same temperature range there are two small peaks at temperature 870 and 919 °C, respectively:

$$\mathrm{Ca}_{10}(\mathrm{PO}_4)_6(\mathrm{OH})_2 \rightarrow \mathrm{Ca}_{10}(\mathrm{PO}_4)_6(\mathrm{OH})_{2-2y}\mathrm{O}_y{\mathrm{V}^{\mathrm{OH}}}_y + y\mathrm{H}_2\mathrm{O} \qquad (6)$$

where V^{OH} denotes the lattice vacancies on OH sites [25,26]:

$$\mathrm{Ca}_{10}(\mathrm{PO}_4)_6(\mathrm{OH})_2 \rightarrow 2\mathrm{Ca}_3(\mathrm{PO}_4)_2 + \mathrm{Ca}_4\mathrm{O}(\mathrm{PO}_4)_2 + \mathrm{H}_2\mathrm{O} \qquad (7)$$

The linear shrinkage (LS) of non-calcined calcium phosphate sample~~s~~ without the presence of CiA, is also illustrated in Fig. 4a. In general, at the temperature range between 750 and 1150 °C, the curve exhibits a bimodal sigmoidal shape. Up to 750 °C there are some small changes of the tablet dimension. The removal of absorbed and/or crystalline water (reaction (3)) takes place initially by expansion and thereinafter by shrinkage of the tablet (Fig. 4c, Table 2, curves 1 and 2, correspondingly). In the broad curve 2, the transformation of acid-phosphate ions to pyrophosphate is also included (reaction (4)). At about 445 °C the sharp peak indicates the crystallization of produced calcium pyrophosphate (CPP) (Fig. 4c, Table 2, curve 3). A small peak at ~665 °C is attributed to the crystallization of α-TCP (Fig. 4c, Table 2, curve 4). The sintering begins (onset temperature) at temperatures 752 °C with a weak endothermic peak (Fig. 4a and c, Table 2, curve 5) corresponding to the reaction (5). The next peak (Fig. 4c, Table 2, curve 6) has maximum linear shrinkage rate at 855 °C is attributed to the endothermic transformation of α-TCP to β-form. Due to the density of α-TCP (2.863 g cm^{-3}, No. 70-0364, ICDD) is smaller than β-form (3.147 g cm^{-3}, No. 70-2065, ICDD) the transformation of α- to β-form leads to the shrinkage of particles. The two previous peaks 5 and 6 are overlapped from the seventh peak (Fig. 4c, Table 2, curve 7) corresponding to pure sintering phenomena. In this temperature range the mechanism of matter transport can be divided in two categories: (a) the reduction of surface area without densification of the material, by superficial diffusion and gaseous phase transport, and (b) the increase of the apparent density, by volume diffusion or grain boundaries. The first mechanism takes place below 850 °C while the second one above 850 °C [35]. The next sigmoidal step consists from two peaks (Fig. 4c, Table 2, curves 8 and 9), the first one is attributed to the reactions (6) and (7), while the second one corresponds to sintering at high temperature. The above reported results are in accordance to our previous paper [25] we found similar behaviour for high crystallinity HA. Generally at lower temperatures, sintering of the primary particles within the agglomerates as well as rearrangement of the agglomerates takes place. At the temperature range between 900 and 1100 °C, the grain growth is controlled by pore mobility, while around 1300 °C rapid grain growth occurs [36]. According to Ruys et al. [37], the HA densification mainly take place between 900 and 1150 °C after what the pore collapse and blowholes appear between 1150 and 1200 °C. Ruys et al. also reported that for temperatures ranging between 1200 and 1350 °C, the blowholes increase in size and number. Mazaheri et al. [38] found that for nanocrystalline HA, a significant densification was observed in a temperature range from 800 to 950 °C. Further increase of the temperature up to 1100 °C, resulted in prohibition of densification mechanisms due to the pressure effect of produced gas in the closed pores followed by the collapse of pores [39]. In contrast, Jokanović et al. [40] concluded that small rate of sintering of the samples sintered at 800 °C, complies with low apparent density and spot-like contacts among the particles, and hence a neck forms between them before particle coalescence occurs. In this case, the sintering process occurs through surface diffusion of vacancies and interstices. In our case, assuming that the densification is related to LS, the linear shrinkage up to ~950 °C was about five folders less (~3.3%) than in the temperature range from 950 to 1190 °C (14.5%).

Table 2
The results of peak separation of differential linear shrinkage curves.

Sample	DTG			DTD		
	Peak number	Peak temperature (°C)	Mass loss (%)	Peak number	Peak temperature (°C)	Linear shrinkage (%)
R0	1	79	1.60	1	69	0.13
	2	128	1.31	2	162	−0.60
	3	187	0.94	3	446	−0.08
	4	293	2.86	4	664	−0.09
	5	812	0.32	5	824	−0.65
	6	1057	0.72	6	855	−0.92
				7	899	−1.75
				8	1031	−5.92
				9	1103	−8.54
				10	1177	0.73
				10a	1202	0.37
R25	1	55	1.14	1	85	0.14
	2	87	3.79	2	133	−0.26
	3	239	3.96	2a	237	−0.22
	4	294	2.63	2b	311	−0.57
	4a	510	2.22	3	–	–
	5	829	0.78	4	658	−1.72
	6	1085	0.87	5	834	−1.20
				6	868	−1.08
				7	892	−6.02
				8 + 9	1079	−32.49
				10	1211	0.88
R50	1	57	0.74	1	77	0.03
	2	99	1.72	2	192	−1.52
	2a	165	0.98	2a	285	−0.06
	3	264	3.68	3	–	–
	3a	316	5.05	4	699	−1.16
	4	485	0.39	5	801	−1.93
	5	787	0.40	6 + 7 + 8	942	−17.22
				9	1053	−3.52
				10	1182	0.28
R75	1	94	2.65	1	51	−0.13
	2	167	4.14	2	150	−0.31
	3	242	5.56	2a	264	−2.37
	3a	374	3.08	3	–	–
	4	497	2.02	4	691	−1.32
	5	831	0.64	5	834	−2.42
	5a	900	0.18	6 + 7 + 9	940	−15.18
	6	966	0.59	8	970	−3.17
				10	1186	0.21
R100	1	90	4.70	1	89	0.04
	2	132	0.29	2	132	−0.36
	3	260	5.19	2a	260	−0.51
	4	342	5.23	3	514	−1.05
	5	786	0.4	4	668	−0.58
				5 + 6	875	−3.00
				7	921	−3.61
				8	1099	−10.51
				9	1183	−1.97

In temperature range between 1170 and 1210 °C two expansion stages were observed (Fig. 4c, Table 2, curves 10 and 10a), with maximum rate of LS at 1177 and 1202 °C, correspondingly. These stages are attributed to the transformation of high density β-TCP to lower density α-form, hence increase of sample volume. This transformation is also observed in the DTA curve by a small endothermic peak at 1187 °C.

The thermal analysis of samples R25, R50, R75 and R100 are depicted in Figs. 5–8, correspondingly. The presence of citrate complexes in the samples results some extra mass loss stages, which are clearly observed in the peak separation of the

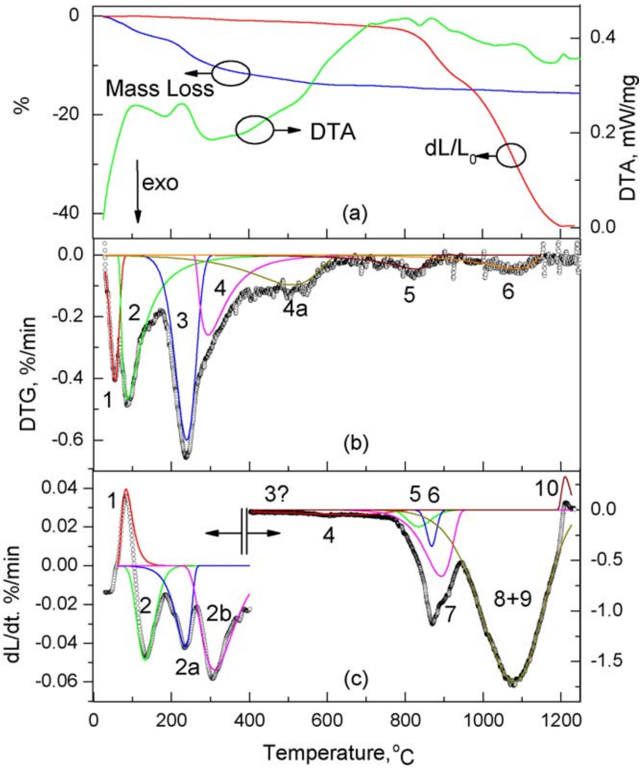

Fig. 5. TG, DTA and linear shrinkage curves (a), as well as the peak separation of DTG (b) and differential linear shrinkage (c) curves of R25 sample.

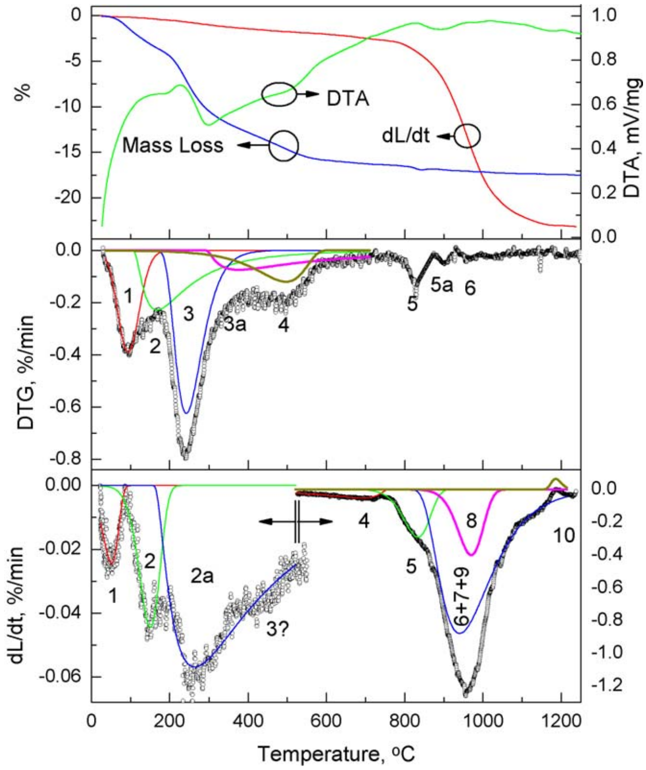

Fig. 7. TG, DTA and linear shrinkage curves (a), as well as the peak separation of DTG (b) and differential linear shrinkage (c) curves of R75 sample.

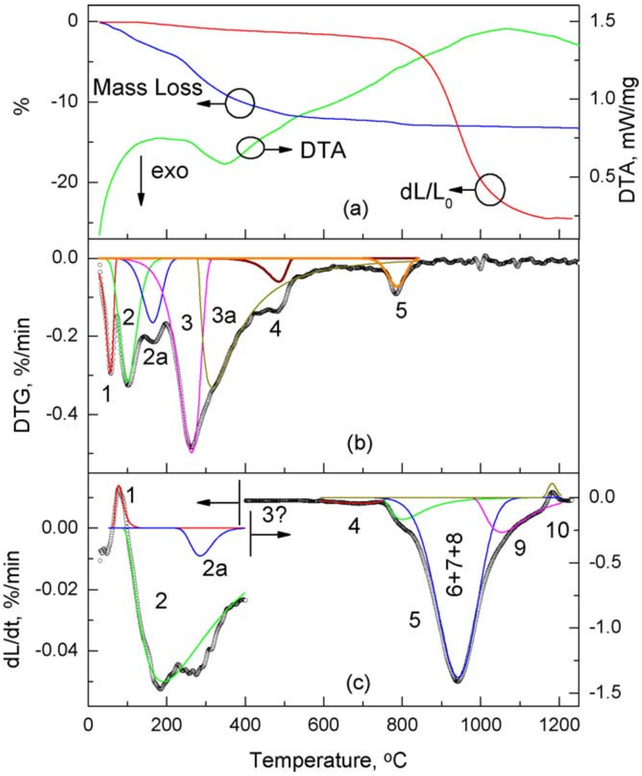

Fig. 6. TG, DTA and linear shrinkage curves (a), as well as the peak separation of DTG (b) and differential linear shrinkage (c) curves of R50 sample.

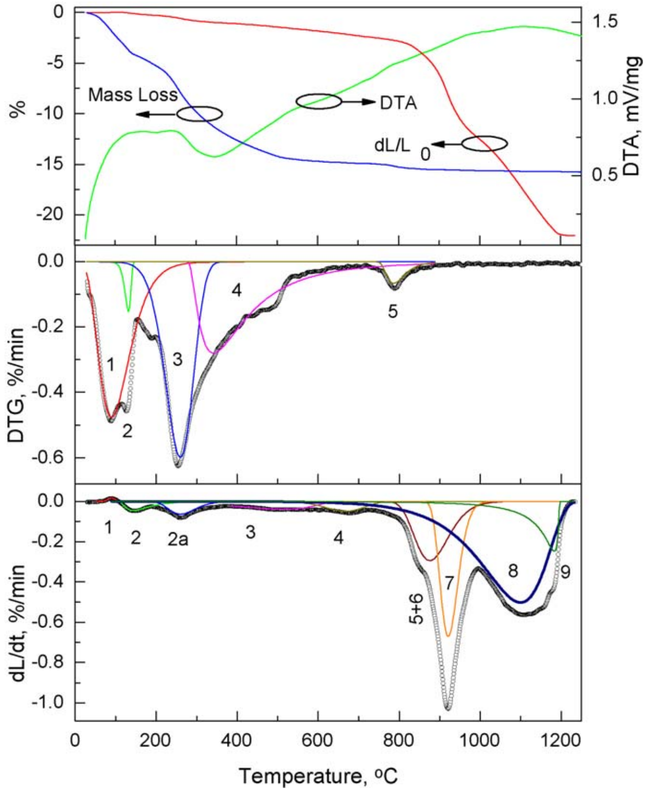

Fig. 8. TG, DTA and linear shrinkage curves (a), as well as the peak separation of DTG (b) and differential linear shrinkage (c) curves of R100 sample.

DTG curves as are shown in the Figs. 5b, 6b, 7b and 8b, as well as in the Table 2. The new stages can be attributed to the decomposition of the produced OCP (reactions (1) and (2)). The absent of a mass loss peak at the temperature range of 900–1000 °C indicate the absent of calcium carbonate phase. The decomposition of calcium citrate in air flow produces $CaCO_3$ (reaction (8)). This reaction is exothermic and appears in the DTA curves of R50, R75 and R100 (Figs. 6a, 7a and 8a) with a broad exothermic peak at the temperature range of 250–500 °C. Consequently the produced $CaCO_3$ react with the OCP, according to reaction (9):

$$(C_6H_5O_7)_2Ca_3 + 9O_2 \rightarrow 3CaCO_3 + 9CO_2 + 5H_2O \qquad (8)$$

$$Ca_8(HPO_4)_2(PO_4)_4 + CaCO_3 \rightarrow 3Ca_3(PO_4)_2 + CO_2 + H_2O \qquad (9)$$

The second step mass loss for all samples, is the sum of the mass loss of 3, 3a, 4 and 4a peaks from the Table 2, that are depicted in Fig. 9. As it seems, the mass loss increases with the increasing the amount of CiA in the initial solution. The samples R25 and R50 show about the same mass loss (8.81 and 9.12%, correspondingly), as well as the samples R75 and R100 (10.66 and 10.42, correspondingly). This behaviour should be related with the results from the XRD patterns, in which the main phase of the calcined samples C25 and C50 is the β-TCP, while for calcined samples C75 and C100 the α-TCP.

The differential linear shrinkage (DLS) curves, as well as their peak separation curves are depicted in Figs. 5c, 6c, 7c and 8c for the samples R25, R50, R75 and R100, respectively. In comparison to the DTG curves, further stages are observed in all DLS curves up to 400 °C. The sharp peak of CPP crystallization at ~450 °C is absent, indicating the formation of crystalline CPP since the beginning of OCP decomposition (reaction (1)). In the above samples the crystallization of the amorphous calcium phosphate (ACP), takes place in the fourth stage with a maximum rate of LS at temperature range between 660 and 690 °C. The corresponding values of %LS are higher than R0 sample, indicating higher amount of amorphous phase.

For the samples prepared in presence of CiA, the main shrinkage occurs also for temperatures above 700 °C. The sample R25 exhibited similar behaviour with the R0 as a function of temperature. The shrinkage stages of R25 sample, also are banded together into two main steps, but with more than two folders linear shrinkage (40.79%, Table 2) from R0 (17.78%, Table 2). The shrinkage stages of the samples R50 and R75 are banded together into only one main step, with total linear shrinkage 22.67 and 20.77%, respectively. In the same temperature range the sample R100 has very different shrinkage behaviour, which takes place in two main steps with total linear shrinkage 19.08%.

In the DTA and DLS curves of samples R25, R50 and R75 the endothermic linear expansion is observed at temperature about 1200 °C, due to the transformation of β-TCP to α-form. The increasing of CiA in the initial solution leads to the decreasing of the %LS and the value of corresponding DTA peak temperature for this stage, indicating a decreasing amount of β-TCP were formed during the precipitation. Remarkable, is the formation of α-TCP in the samples R75 and R100 after calcinations at 900 °C, and the absent of the above peak on the DTD curve of the last one.

3.4. Textural analysis

The adsorption isotherms of uncalcined samples are shown in Fig. 10, while the specific surface area (SSA) in Table 1. All the adsorption isotherms have the same shape, which is attributed to type III characteristic for nonporous solids. The hysteris loops indicate the appearance of mesopores due to the interspaces between the particles in the aggregates. The specific surface area of sample in absence of CiA in the initial solution was 60 m^2/g. The presence of CiA in the initial solution resulting to increase the SSA significantly. The SSA increases from 109 to 172 m^2/g as the amount of CiA in the initial solution increased. The SSA of the samples shows significant differences after calcination at 900 °C. The SSA of samples prepared in absence of CiA after calcination increases (82 m^2/g). On the contrary, the presence of OCP in the as prepared samples results to a dramatically decrease

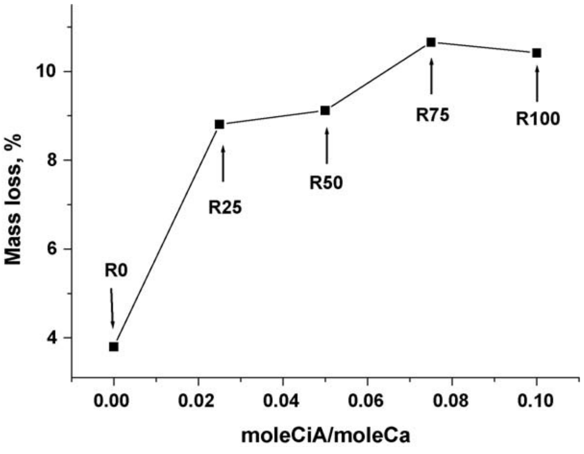

Fig. 9. The mass loss of the second steps of the samples.

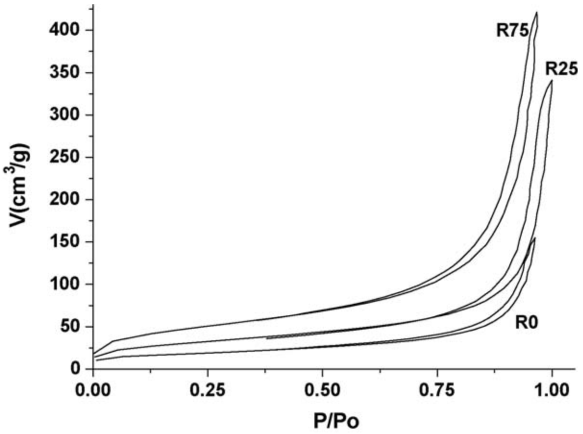

Fig. 10. N_2 adsorption and desorption isotherms expressed as volumes of gas vs. partial pressure. The collected isotherms are suggestively from the uncalcined samples R0, R25 and R75.

of SSA after calcination from 10 to 2 m^2/g as the amount of OCP increases.

Fig. 11 shows SEM micrographs of uncalcined samples. The sample R0 consists of needle-like particles. The main size of the individual particles is estimated to be around 200–300 nm in length and 50 nm in width. The precipitated samples from the solutions which content CiA, are consisted of big aggregates of small particles, due to the presence of substantial amount from calcium citrate complexes. The shape of small particles is spheroidal with mean diameter around 100–200 nm. These results indicate that citrate absorbs on the calcium phosphate nuclei, inhibits their growth and finally leading to the formation of a large number of small particles which contribute to a higher surface area [32]. On the other hand, the calcium citrate complexes acting as template of the heterogeneous nucleation of calcium phosphate, producing uniform fine particles [41,42]. Martins et al. [34] found that when the initial pH increased above 8, the particle size decreases dramatically. In our case, after the ammonia addition, the pH of the solution became about 8.8. The agglomerate free spherical shape particles are more advantageous for the fabrication of homogeneous green compacts. The spherical particle morphology is also important for decreasing the interparticle frictional forces during the pressure assisted densification [36].

These nanometer-sized particles have high surface energy and could be sintered from the onset of thermal crystallization at temperature 600 °C, compacted with the crystalline HA powder, which has shown shrinkage and the formation of grain boundaries only at 1100 [28]. The high specific surface area of the smaller particles often accounts for their high reactivity and driving force for sintering [36]. Microporosity is usually obtained by using low sintering temperatures. Microporous CaP ceramics have been easily prepared starting from amorphous CaP powders [43,44].

Fig. 12 shows SEM micrographs of calcined samples at 900 °C. The calcination of sample without additives (C0), consists of tufts of needle-like particles, that indicates the beginning of sintering. The size of the individual particles is estimated to be around 500–1000 nm long. On the contrary, in the samples with the presence of calcium citrate, the sintering

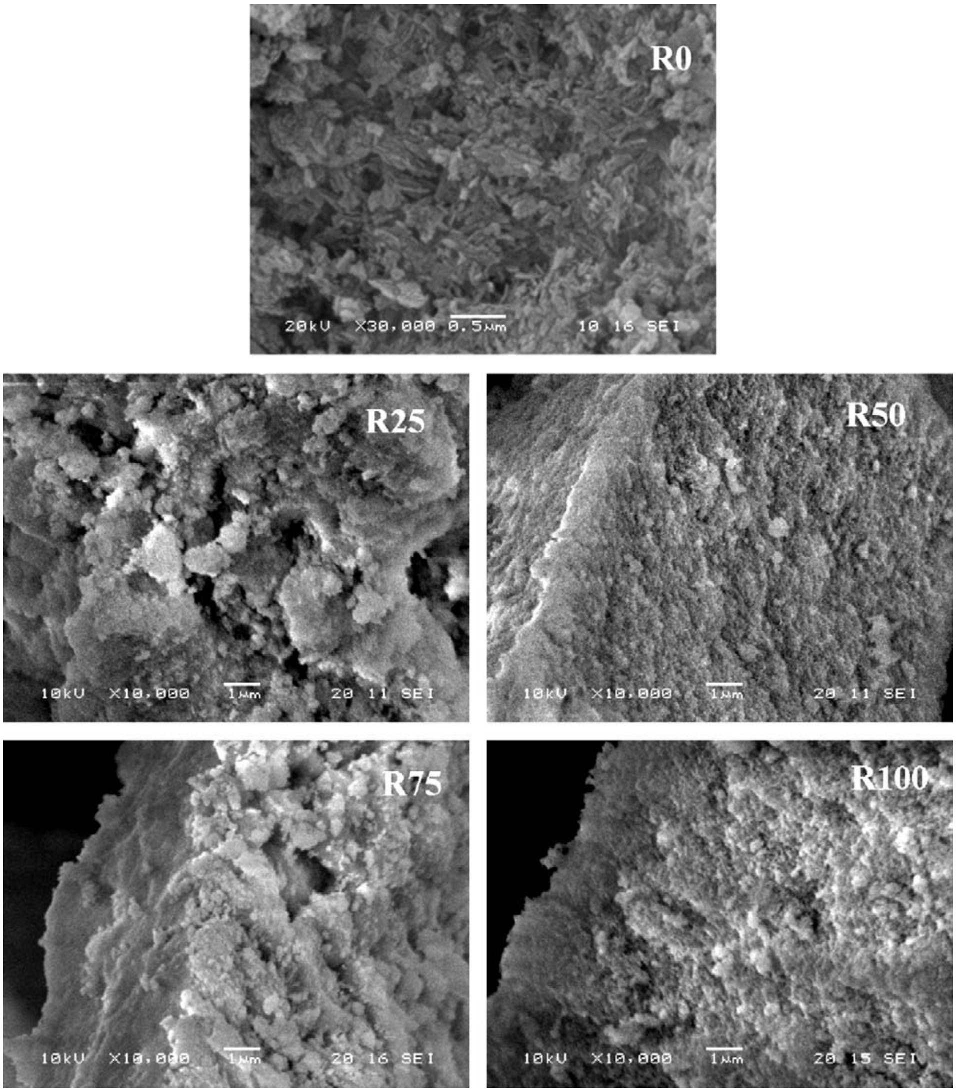

Fig. 11. SEM microphotograph of uncalcined samples.

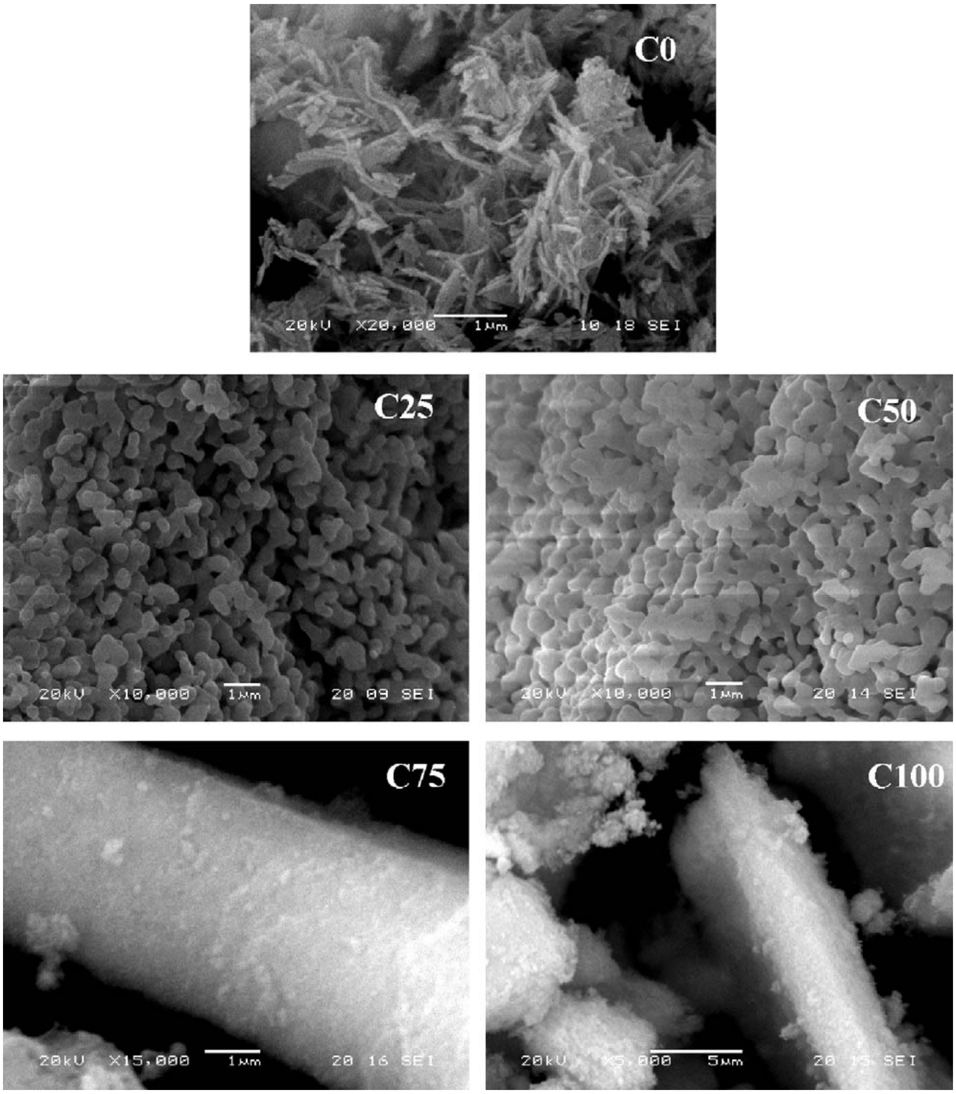

Fig. 12. SEM microphotograph of calcined samples.

was more obvious. Thermal treatment of samples R25 and R50 (calcined samples C25 and C50, respectively) at temperature of 900 °C has as a result a particle joining in a concave neck, leaving a network of open large pores throughout the entire ceramic, which had a denser structure. This surface diffusion began after about 500 °C, which corresponds to the crystallization of the amorphous powders. The samples with higher content of calcium citrate (R75 and R100), after calcination (C75 and C100, correspondingly) produce very large non-porous particles. The sintering behaviour depends not only on the particle size but also on the particle morphology, because a large particle size along with hard agglomerates exhibits lower densification. On the other hand, the difference in shrinkage between the agglomerates is also responsible for the production of small cracks and other kinds of three-dimensional defects (closed pores entrapped between the intersections of different grains) in the sintered HA [45–47]. The aggregation of uncalcined particles is ruled by surface energy minimization [41], facilitate the sintering process. The observations from SEM micrographs are in accordance with the BET results.

According to Martins et al. [34] the citrate ions mobilize calcium ions as calcium–citrate complexes, most probably as $CaCit^-$ and CaHCit species and are introduced in the precipitating medium during the first steps of the starting reagents mixture process. On the other hand, the precipitation of biphasic low crystallinity small particles suggests a growth mechanism involving an aggregation step of smaller primary crystal units rather than single-crystal growth. In alkaline pH range, mainly exist as anionic citrate species, which may adsorb on the precipitated particles' surface. Hence produce an overall negative surface charge preventing not only the primary unit particle growth but also their aggregation. HA that crystallizes with a hexagonal structure has different spatial arrangements of calcium and phosphate groups. The rectangular *ac* or *bc* crystal facets are rich in calcium ions or positive charge and consequently the citrate ions will adsorb preferentially onto these facets, thus giving rise to electrostatic inhibition of rectangular facet-to-facet particle aggregation.

High pH values and high temperature favour the dissolution of CiA, thus the Ci^{3-} ions are presented mainly in the solution, which are adsorbed on the solid surface might account for the development of the higher negative surface charge of nanoparticles than the less negative and less abundant $HCit^{2-}$ ions. Therefore the formation of nanometric particles from calcium/citrate/phosphate solutions is here proposed as a result from three main contributions: (a) a high supersaturation established at an appropriate pH condition after the addition of ammonia solution, (b) an inhibition of the primary units aggregation, owed to their high particle surface charge due to the Ci^{3-} ions adsorption, and (c) the concentration of Ci^{3-} ions. However, the solution pH decreases as the particle growth proceeds, thereby increasing the concentration of $HCit^{2-}$ and $CaCit^{-}$ species [34]. Such species prompt the complexation between the –COO– groups and calcium ions ($–COO–Ca^{2+}–OOC–$), which are being incorporated into the solid structure during particle growth. These phenomena enable the adhesion of neighbour particles, and the precipitated solids consist from nanometric particles.

4. Conclusion

The modified precipitation method leads to the formation of biphasic needle-like particles consisted of crystalline HA and β-TCP. The presence of CiA in the initial solution acts as an entrapping agent leading to the formation of low crystallinity phases of HA and OCP with lower Ca/P atomic ratio than TCP. In all cases the ceramics were aggregated nonporous small spheroidal particles. After calcination, the formation of α-TCP is attributed to the idiomorphic structure of the uncalcined sample, due to the presence of a large amount of calcium citrate complexes. The main sintering process takes place at the temperature range between 750 and 1150 °C. The number of sintering stages as well as the %LS of them, were strongly depended on the amount of the CiA during the precipitation, due to the different composition of raw precipitated materials. The presence of OCP and calcium citrate complexes in the raw materials, facilitates the sintering process, resulting to a dramatic decrease of specific surface area of the calcined ceramics.

The observed differences of particle size and morphology indicate a strong influence of the solution speciation on the nucleation and growth processes. The formation of nanometric particles from calcium/citrate/phosphate solutions is proposed as a result from the high supersaturation established after the addition of ammonia solution, the inhibition of the primary unit aggregation, and the concentration of Ci^{3-} ions. The presence of $HCit^{2-}$ and $CaCit^{-}$ species in the solution prompt the complexation and incorporation into the solid structure during particle growth, and thus inhibit the aggregation of neighbour particles.

References

[1] A. Wang, S. Liu, H. Yin, H. Wu, Y. Wada, M. Ren, T. Jiang, X. Cheng, Y. Xu, Size-controlled synthesis of hydroxyapatite nanorods by chemical precipitation in the presence of organic modifiers, Mater. Sci. Eng. C 27 (2007) 865–869.

[2] Y. Han, S. Li, X. Wang, X. Chen, Synthesis and sintering of nanocrystalline hydroxyapatite powders by citric acid sol–gel combustion method, Mater. Res. Bull. 39 (2004) 25–32.

[3] J. Liu, K. Li, H. Wang, M. Zhu, H. Yan, Rapid formation of hydroxyapatite nanostructures by microwave irradiation, Chem. Phys. Lett. 396 (2004) 429–432.

[4] G. Guo, Z. Wang, H. Guo, Preparation of hydroxyapatite nanoparticles by reverse microemulsion, Ceram. Int. 31 (2005) 869–872.

[5] A. Milev, G.S.K. Kannangara, B. Ben-Nissan, Morphological stability of hydroxyapatite precursor, Mater. Lett. 57 (2003) 1960–1965.

[6] L. Yan, Y. Li, Z. Deng, J. Zhuang, X. Sun, Surfactant-assisted hydrothermal synthesis of hydroxyapatite nanorods, Int. J. Inorg. Mater. 3 (2001) 633–637.

[7] D.N. Misra, Interaction of citric acid with hydroxyapatite: surface exchange of ions and precipitation of calcium citrate, J. Dent. Res. 75 (1996) 1418–1425.

[8] H. Liu, H. Li, W. Cheng, Y. Yang, M. Zhu, C. Zhou, Novel injectable calcium phosphate/chitosan composites for bone substitute materials, Acta Biomater. 2 (2006) 557–565.

[9] K.J. Westin, A.C. Rasmuson, Nucleation of calcium carbonate in presence of citric acid, DTPA, EDTA and pyromellitic acid, J. Colloid Interface Sci. 282 (2005) 370–379.

[10] N. Spanos, A. Patis, D. kanellopoulos, N. Andritsos, P.G. Koutsoukos, Precipitation of calcium phosphate from simulated milk ultrafiltration solutions, Cryst. Growth Des. 7 (2007) 25–29.

[11] S.K. Pratihar, M. Garg, S. Mehra, S. Bhattacharyya, Phase evolution and sintering kinetics of hydroxyapatite synthesized by solution combustion technique, J. Mater. Sci. Mater. Med. 17 (2006) 501–507.

[12] J. Zhang, X. Gao, B. Song, Z. Wang, W. Lu, A novel technique to synthesize hydroxyapatite whiskers, Mater. Lett. 62 (2008) 1162–1164.

[13] A. Wang, H. Yin, D. Liu, H. Wu, Y. Wada, M. Ren, Y. Xu, T. Jiang, X. Cheng, Effects of organic modifiers on the size-controlled synthesis of hydroxyapatite nanorods, Appl. Surf. Sci. 253 (2007) 3311–3316.

[14] C. Li, F. Meng, Nano-crystallinite hydroxyapatite synthesized by neutralization with the assist of citric acid, Mater. Lett. 62 (2008) 932–934.

[15] R. Jenness, J. Koops, Preparation and properties of a salt solution which simuleates milk ultrafiltrate, Netherlands Milk Diary J. 16 (1962) 153–164.

[16] R. Rosmanindo, L.F. Melo, The effect of citrate on calcium phosphate deposition from simulated milk ultrafitratie (SMUF) solution, J. Food Eng. 73 (2006) 379–387.

[17] C.L. Chu, P.H. Lin, S. Dong, D.Y. Guo, Influences of citric acid as a chelating reagent on the characteristics of nanophase hydroxyapatite powders fabricated by a sol–gel method, J. Mater. Sci. Lett. 21 (2002) 1793–1795.

[18] W. Weng, G. Han, P. Du, G. Shen, The effect of citric acid addition on the formation of sol–gel derived hydroxyapatite, Mater. Chem. Phys. 74 (2002) 92–97.

[19] J. Torrent-Burgués, J. Gómez-Morales, A. López-Macipe, R. Rodríquez-Clemente, Continuous precipitation of hydroxyapatite from Ca/citrate/phosphate solutions using microwave heating, Cryst. Res. Technol. 34 (1999) 757–762.

[20] H.Y. Juang, M.H. Hon, Effect of calcination on sintering of hydroxyapatite, Biomaterials 17 (1996) 2059–2064.

[21] S. Best, W. Bonfield, Processing behaviour of hydroxyapatite powders with contrasting morphology, J. Mater. Sci. Mater. Med. 5 (1994) 516–521.

[22] C. Kothapalli, M. Wei, A. Vasiliev, M.T. Shaw, Influence of temperature and concentration on the sintering behavior and mechanical properties of hydroxyapatite, Acta Mater. 52 (2004) 5655–5663.

[23] R.Z. LeGeros, J.P. LeGeros, Dense hydroxyapatite, in: L.L. Hench, J. Wilson (Eds.), An Introduction to Bioceramics, World Scientific, Singapore, 1993, pp. 139–180.

[24] N.Y. Mostafa, Characterization, thermal stability and sintering of hydroxyapatite powders prepared by different routes, Mater. Chem. Phys. 94 (2005) 333–341.

[25] G.C. Koumoulidis, C.C. Trapalis, T.C. Vaimakis, Sintering of hydroxyapatite lath-like powders, J. Therm. Anal. Calorim. 84 (2006) 165–174.

[26] G.C. Koumoulidis, T.C. Vaimakis, A.T. Sdoukos, N.K. Boukos, C.C. Trapalis, Preparation of hydroxyapatite lathlike particles using high-speed dispersing equipment, J. Am. Ceram. Soc. 84 (2001) 1203–1208.

[27] References 92 and 328 in J. Elliott, Structure and Chemistry of the Apatites and Other Calcium Orthophosphates, Elsevier, London, 1994, p. 55.

[28] B.H. Fellah, P. Layrolle, Sol–gel synthesis and characterization of macroporous calcium phosphate bioceramics containing microporosity, Acta Biomater. 5 (2009) 735–742.

[29] Reference 146 in J. Elliott, Structure and Chemistry of the Apatites and Other Calcium Orthophosphates, Elsevier, London, 1994, p. 55.

[30] W.H. Monma, M. Nagai, Calcium orthophosphates, in: T. Kanazawa (Ed.), Inorganic Phosphate Materials, Elsevier, Tokyo, 1989, pp. 86–87.

[31] J.C. Elliott, Structure and Chemistry of Apatites and Other Calcium Orthophosphates, Elsevier, 1994, pp. 36–37.

[32] K.S. Tenhuisen, P.W. Brown, The effects of citric and acetic acids on the formation of calcium-deficient hydroxyapatite at 38 °C, J. Mater. Sci. Mater. Med. 5 (1994) 291–298.

[33] J.E. Barralet, M. Tremayne, K.J. Lilley, U. Gbureck, Modification of calcium phosphate cement with α-hydroxy acids and their salts, Chem. Mater. 17 (2005) 1313–1319.

[34] M.A. Martins, C. Santos, M.M. Almeida, M.E.V. Costa, Hydroxyapatite micro- and nanoparticles: nucleation and growth mechanisms in the presence of citrate species, J. Colloid Interface Sci. 318 (2008) 210–216.

[35] D. Bernache-Assollant, A. Ababou, E. Champion, M. Heughebaert, Sintering of calcium phosphate hydroxyapatite $Ca_{10}(PO_4)_6(OH)_2$. I. Calcination and particle growth, J. Eur. Ceram. Soc. 23 (2003) 229–241.

[36] R. Chaim, M. Levin, A. Shlayer, C. Estournes, Sintering and densification of nanocrystalline ceramic oxide powders: a review, Adv. Appl. Ceram. 107 (2008) 159.

[37] A.J. Ruys, M. Wei, C.C. Sorrell, M.R. Dickson, A. Brandwood, B.K. Milthorpe, Sintering effects on the strength of hydroxyapatite, Biomaterials 16 (1995) 409–415.

[38] M. Mazaheri, M. Haghighatzadeh, A.M. Zahedi, S.K. Sadrnezhaad, Effect of a novel sintering process on mechanical properties of hydroxyapatite ceramics, J. Alloys Compd. 471 (2009) 180–184.

[39] M. Mazaheri, A.M. Zahedi, S.K. Sadrnezhaad, Two-step sintering of nanocrystalline ZnO compacts: effect of temperature on densification and grain growth, J. Am. Ceram. Soc. 91 (2008) 56–63.

[40] V. Jokanović, B. Jokanović, D. Marković, V. Živojinović, S. Pašalić, D. Izvonare, M. Plavšić, Kinetics and sintering mechanisms of hydro-thermally obtained hydroxyapatite, Mater. Chem. Phys. 111 (2008) 180–185.

[41] R. Rodríquez-Clemente, A. López-Macipe, J. Gómez-Morales, J. Torrent-Burgués, V.M. Castaňo, Hydroxyapatite precipitation: a case of nucleation–aggregation–agglomeration–growth mechanism, Eur. Ceram. Soc. 18 (1998) 1351–1356.

[42] A. López-Macipe, J. Gómez-Morales, R. Rodríquez-Clemente, Nanosized hydroxyapatite precipitation from homogeneous calcium/citrate/phosphate solutions using microwave and conventional heating, Adv. Mater. 10 (1998) 49–53.

[43] B.H. Fellah, P. Weiss, O. Gauthier, T. Rouillon, P. Pilet, G. Daculsi, et al., Bone repair using a new injectable self-crosslinkable bone substitute, J. Orthop. Res. 24 (2006) 628.

[44] P. Layrolle, A. Lebugle, Characterization and reactivity of nanosized calcium phosphates prepared in anhydrous ethanol, Chem. Mater. 6 (1994) 1996–2004.

[45] S.R. Kim, J.H. Lee, Y.T. Kim, D.H. Riu, S.J. Jung, Y.J. Lee, S.C. Chung, Y.H. Kim, Synthesis of Si, Mg substituted hydroxyapatites and their sintering behaviours, Biomaterials 24 (2003) 1389–1398.

[46] E. Bertoni, A. Bigi, G. Cojazzi, M. Gandolfi, S. Panzavolta, N. Rover, Nanocrystals of magnesium and fluoride substituted hydroxyapatite, J. Inorg. Biochem. 72 (1998) 29–35.

[47] A. Banerjee, A. Bandyopadhyay, S. Bose, Hydroxyapatite nanopowders: synthesis, densification and cell–materials interaction, Mater. Sci. Eng. C 27 (2006) 729–735.